Journal of CO2 Utilization 112 (2026) 103561

Contents lists available at ScienceDirect

Journal of CO2 Utilization

journal homepage: www.elsevier.com/locate/jcou

On the role of the binding agent in silver-based low-temperature electroreduction of CO_2 to CO with flowing aqueous electrolyte

Simon Emken [a,b], Kristina Froehlich [a], Alexander Bauer [a,*], Eva Jodat [a], André Karl [a], Rüdiger-A. Eichel [a,b,c]

[a] Institute of Energy Technologies, Fundamental Electrochemistry (IET-1), Forschungszentrum Jülich, Jülich, 52425, Germany
[b] Institute of Physical Chemistry, RWTH Aachen University, Aachen, 52062, Germany
[c] Faculty of Mechanical Engineering, RWTH Aachen University, Aachen, 52062, Germany

ARTICLE INFO

Keywords:
CO_2 electrolysis
Gas diffusion electrodes
Silver electrocatalysts
Ionomer
Binding agent

ABSTRACT

In this study, the role of the binding agent in the silver-based low-temperature electroreduction of carbon dioxide (CO_2) to carbon monoxide (CO) was investigated by comparing silver nanoparticle-based gas diffusion electrodes (GDEs) prepared by ultrasonic spray coating with binding agents that are most frequently applied in this field of study. The GDEs were analyzed electrochemically using cyclic voltammetry (CV) and electrochemical impedance spectroscopy (EIS), and tested in galvanostatic flow cell experiments at a current density of -200 mA•cm^{-2} for 2 h. The electrochemical analysis revealed strong effects on the double-layer capacitance as well as the charge transfer resistance, depending on the type of binder used. In flow cell experiments, the selectivity of the electroreduction was mainly determined by the hydrophobicity of the binding agent. Furthermore, post-test laser scanning microscopy (LSM) and scanning electron microscopy (SEM) imaging showed that the mechanical stability of the catalyst layer was largely affected by the binding agent.

1. Introduction

CO_2 electroreduction has attracted increasing research interest in the past decade due to its potential application in defossilizing the chemical industry and hard-to-abate sectors via Power-to-X vectors [1–3]. CO_2 electroreduction to CO is of particular interest due to its comparatively favorable economic prospects and the wide range of application of CO in the chemical industry [2,4,5]. Silver is the most promising electrocatalyst for the scale-up of CO_2-to-CO conversion processes [6–14]. Recently, the importance of the GDE fabrication methodology on the performance of CO_2 electroreduction has been increasingly acknowledged [15–19]. The binding agent is an integral part of most inks used to prepare silver-based catalyst layers, which can be an ion-conducting polymer (ionomer) or a non-conducting one. In the latter case, perfluorinated polymers like polytetrafluoroethylene (PTFE) are commonly applied [20,21]. The binding agent can control the microenvironment of the silver catalyst, which is recognized as one of the decisive factors determining the selectivity of the electroreduction process [17,22–24]. Despite the aforementioned increased attention towards the role of the binding agent, systematic studies investigating their effects on the silver-based electroreduction are still scarce[25].

A summary of recent studies that report on different binding agents or ionomers in catalyst layers is provided in Table 1 to assess the current understanding of the role of binding agents with respect to the CO_2 electroreduction performance of GDEs. Despite differences in catalyst materials, catalyst layer compositions, ionomer chemistry, and electrolyzer configurations, several common trends can be identified. First, the choice of binding agent can substantially affect product selectivity. In particular, hydrophilicity appears to be an important parameter, with more hydrophilic binding agents generally being associated with increased FE(H_2) in catholyte-gap-type cells[26]. For example, in a comparison of Sustainion, PiperION, and Nafion as binding agents for silver nanoparticles, the PiperION-based GDE with the lowest contact angle exhibited a substantially higher FE(H_2) of approximately 15%, compared with less than 5% for the Nafion- and Sustainion-based GDEs [27]. Similarly, Nafion incorporation into copper-based electrodes has been reported to suppress FE(H_2) compared with a bare copper electrode [28]. In another study, in which eight binding agents for a copper electrocatalyst were compared for CO electroreduction, the three GDEs with the lowest contact angles (<10°, compared with >110° for the

* Corresponding author.
E-mail address: a.bauer@fz-juelich.de (A. Bauer).

https://doi.org/10.1016/j.jcou.2026.103561
Received 21 July 2026; Received in revised form 2 September 2026; Accepted 7 September 2026
Available online 14 September 2026

remaining GDEs) exhibited the highest FE(H_2), exceeding 70% compared with less than 35% for the more hydrophobic GDEs[29]. Together, these studies suggest that increased hydrophilicity and the associated enhanced water availability within the catalyst layer can promote the competing hydrogen evolution reaction. Second, the binding agent content can also influence the product distribution. Increasing the ionomer content generally seems to result in an increase in FE(H_2), although the magnitude of this effect depends on the catalyst and electrode architecture[30]. For example, in bismuth-based GDEs, decreasing the catalyst-to-Nafion ratio from 70:30–30:70 at a constant catalyst loading of 0.75 mg•cm^{-2} resulted in an increase in FE(H_2) from less than 5% to more than 60%[31]. Third, the effect of a ionomer can depend strongly on the electrolyzer configuration. For example, PiperION was reported to increase FE(H_2) in catholyte-gap cells, whereas low FE(H_2) and favorable CO_2-reduction performance were reported for PiperION in zero-gap or membrane-electrode-assembly configurations [8,32,33]. In one comparison of silver-based GDEs operated in a zero-gap electrolyzer, the PiperION-based GDE exhibited an FE(H_2) of only 12% at 300 mA•cm^{-2}, compared with 29% for the corresponding Nafion-based GDE[34]. This behavior is in contrast with the increased FE(H_2) observed for PiperION in catholyte-gap configurations and indicates that the effect of an ionomer cannot be considered independently of the electrolyzer architecture and associated transport conditions.

Despite these reported effects, direct comparisons of different ionomers with otherwise identical catalyst layer compositions and electrolysis conditions remain limited. In particular, the individual contributions of ionomer hydrophilicity, water uptake, ionic conductivity, and catalyst layer stability are difficult to disentangle from the available literature, as differences in catalyst loading, ionomer content, electrode architecture, and electrolyzer configuration often occur simultaneously. Therefore, a systematic comparison under controlled conditions is required to clarify the role of the ionomer in Ag-based GDEs, which is the aim of this study. To address the lack of a systematic comparison of binding agents in silver-based GDEs for the electroreduction of CO_2 to CO, the most frequently applied binding agents identified in a recently published literature analysis (Figure S1) were selected for the preparation of silver nanoparticle-based GDEs[41]. The resulting GDEs were systematically characterized by cyclic voltammetry (CV) and electrochemical impedance spectroscopy (EIS), followed by galvanostatic electrolysis in a flow cell using aqueous $KHCO_3$ electrolyte at −200 mA•cm^{-2} for 2 h. By correlating the electrochemical and electrolysis performance with ionomer properties, including ionic conductivity, water uptake, and wettability, this study aims to elucidate the influence of the ionomer on the electrochemical behavior, product selectivity, and stability of silver-based GDEs.

2. Materials and methods

2.1. Materials

Silver nanoparticles (IoLiTec nanomaterials, NM-0038-UP-0005, 50–60 nm, 99.9%), Sigracet 36BB gas diffusion layers (Ion Power GmbH), and $KHCO_3$ (Fisher Scientific, 450640050, p.a.) were used as received. The solvents ethanol (Carl Roth, 9065.2, Rotipuran >99.8% p.a.) and acetone (Honeywell, 179973, >99.5%) to prepare the catalyst inks were used without further purification. The binding agents Nafion D-520CS (Ion Power GmbH, 5 wt% in water/lower alcohol mixture), Aquivion D72–25BS (Sigma Aldrich, 802549–25 ml, 25 wt% in H_2O), PTFE (Sigma Aldrich, 665800–100 ml, 60 wt% dispersion in H_2O), Fumion FAA-3-solut-10 (Fuel Cell Store, 8–12(10) wt% in N-methyl-2-pyrrolidone (NMP)), Sustainion XA - 9 (Dioxide Materials, 5 wt% in ethanol), PiperION (Fuel Cell Store, 72020001, 5 wt% in organic solvent (undisclosed)), Aemion + AP3-HNN9 (Ionomr Innovations Inc., solid) were used as delivered and diluted to ~5 mg•g^{-1} stock solutions in ethanol (Nafion, Aquivion, Fumion, Sustainion, PiperION), a 1 mg•g^{-1} stock solution in EtOH:Acetone 65:35 (wt/wt) (Aemion) and a 5 wt% stock solution in H_2O (PTFE). Ultrapure water from an Elga Purelab Flex 3 M2 purification system was used to prepare the PTFE stock solution and the 2 M $KHCO_3$ electrolyte. The IrO_2-coated membrane electrode assembly (1/2 MEA, membrane coated on one side only, Ion Power GmbH, HYDRion™ Membrane N115, IrO_2 1 mg•cm^{-2}, thickness 116.84 −137.16 µm, 5 ×5 cm^2 coated area, 8 ×8 cm^2 overall dimensions)[42] was used for multiple experiments and stored in ultrapure water between experiments. Before the start of the experimental campaign, it was stored in ultrapure water for more than one day.

2.2. Electrode preparation

Gas diffusion electrodes with Ag nanoparticles and ionomer/binding agent containing catalyst layers, as well as pure ionomer coatings, were fabricated by spraying the respective inks onto Sigracet 36BB gas diffusion layers (GDL) using a Nadetech ND-SP ultrasonic spray coater

Table 1
Studies focusing on the effects of different binding agents/ionomers in low-temperature CO_2 electroreduction.

Reference	Electrocatalyst	Main product	Cell type	Catholyte	Findings
Nwabara et al. [35]	Ag	CO	GDE	2 M KOH	Large differences in R_{ct} between PTFE-, Sustainion- and Nafion-based catalyst layers
Gonugunta et al.[36]	Ag	CO	GDE	$KHCO_3$	Best performance with polypyrrole as binding agent
Abarca et al. [31]	$(BiO)_2CO_3$ and Bi_2O_3	HCOOH	GDE	$KHCO_3$	Loading effect: Increase in FE(H_2) for Nafion content > 50% due to blockage of CO_2 diffusion pathways
Chang et al. [37]	Cu	C_{2+}	GDE	$KHCO_3$	Sustainion increases FE(CO) and decreases FE(C_{2+}) due to charge-transfer with Cu surface: Reduced CO adsorption
Yu et al.[27]	Ag, CoPc, PTFE in all catalyst layers	CO	GDE	$KHCO_3$	Increased FE(H_2) for PiperION compared to Sustainion and Nafion, GDE without binding agent (only PTFE) most stable in extended lab experiment
Kim et al.[28]	Cu	C_{2+}	GDE	$LiHCO_3$ and $CsHCO_3$	Nafion: Suppressed hydrogen evolution
Galbicsek et al. [29]	Cu	C_{2+} (CO electroreduction)	Microfluidic	KOH	Hydrophilic binding agents: Increased FE(H_2)
Seteiz et al.[30]	Ag supported on carbon black	CO	MEA	-	Increasing FE(H_2) for increasing PiperION content from 5 to 45 wt%
Liu et al.[38]	Ag supported on carbon black	CO	MEA	-	FE(H_2)(Fumion) < FE(H_2)(Nafion), Fumion enabled perspiration of electrolyte
Jung et al.[39]	Ag	CO	H-cell, MEA	-	Lower water uptake of ionomers beneficial for suppression of FE(H_2)
Zeng et al.[40]	Cu	C_{2+}	MEA	-	Hydrophobicity is the decisive factor for product selectivity. Decreasing hydrophobicity increases FE(H_2)
Gatti et al.[34]	Ag	CO	MEA	-	FE(H_2) increases for different binders in the order of Sustainion < PiperION < Fumion < Nafion

equipped with an ultrasonic nozzle[41].

The Sigracet 36BB GDLs were cut into 6.5 × 7.0 cm^2 pieces for spraying using a STAR MA3 manual hydraulic press (Lucris Manufacturing) and weighed before the spraying process using an analytical balance. The inks were prepared by adding silver nanoparticles to ethanol (Fumion, Sustainion, PiperION, Nafion, Aquivion, PTFE) or ethanol:acetone 65:35 (wt/wt) solvent mixtures (Aemion) and adding the necessary amount of the binding agent stock solution/dispersion [43,44]. The total ink volume was 20 ml. The necessary amount of binding agent in the ink was calculated based on the deposition efficiency (see Table S1) of the binding agent, which was determined by spraying 20 mg of the binding agent in an ethanol or ethanol-acetone solvent mixture (for Aemion) onto Sigracet 36BB GDLs using the same spraying recipe and substrate dimensions. Before spraying, the inks were treated with a Hielscher UP100H sonotrode MS2 at 0.9 cycles (0.9 s pulse, 0.1 s break) and 75% power for 30 min to ensure a homogeneous dispersion of the silver nanoparticles. In a 10 min interval the ink was left to cool in a water bath for approximately 5 min. For spraying, the ultrasonicated ink was drawn into a 20 ml Henke-Ject syringe, which was mounted into position in the ultrasonic spray coater. The full area (6.5 ×7.0 cm^2) of the GDL was sprayed with the pre-defined rectangle design by Nadetech (with 55 ×60 mm^2 dimensions) at 0.75 bar air pressure, 400 mm•min^{-1} speed, 5 s spraying stabilization time, and 20.0 ml•h^{-1} working flow. For the spray pattern, the "distance between steps" was set to 4 mm, and the "stabilized spraying distance" and "overage distance step" parameters were set to 5 mm and 3 mm, respectively. The nozzle-to-substrate distance was 60 mm and the spraying process was operated at ambient temperature (22 ± 2 °C) without making use of the heating plate. The configuration resulted in a minimal loss of ink due to spraying outside of the edges of the electrode substrate (see Figure S5) and in 20–22 layers during a total spraying time of ~65–70 min. The same spraying recipe was used for the fabrication of all electrodes except for the Aemion GDEs, as in that case, the significantly lower viscosity of the ethanol/acetone mixture led to increased agglomeration and sedimentation of the silver catalyst (see Table S3 and Figure S29). For the Aemion GDEs, the working flow was increased to 30 ml•h^{-1} and the ink volume was reduced to 18 ml. After drying for at least 1 h, the GDEs were weighed on an analytical balance to calculate the mass loading of the two solids (silver nanoparticles and binding agent) that were dispersed and dissolved in the ink. The GDEs with PTFE as a binding agent were heat-treated in a tube furnace (Carbolite Gero) in an Ar atmosphere at 250 °C for 2 h with a heating rate of 2 K•min^{-1} according to a methodology adopted from the literature[35]. The catalyst + binding agent loading was ~1.85 mg•cm^{-2} and the binding agent content was ~8.5 wt% with respect to the catalyst mass as reported in Table S2 and Table S3 in the Supporting Information.

2.3. Cell setup

A flow chart of the cell setup, a photograph of the experimental setup, as well as a scheme of the electrochemical cell are given in Figure S6 in the supporting information. The setup consisted of a commercial flow cell (Gaskatel GmbH, ElyFlow, 83400 [45,46]) featuring a geometric electrode area of 10 cm^2, a 400 ml PTFE electrolyte vessel connected to a PP membrane pump (Gaskatel GmbH, 83721), which was used for catholyte circulation, a humidifier, and a pressure control system. The ElyFlow cell consisted of two 10 mm wide analyte compartments of 25 ml volume, with Haber-Luggin capillaries for reference electrodes. The IrO_2-coated membrane electrode assembly was placed between the analyte compartments The counter electrode holder was equipped with a mixed metal oxide (MMO) anode (64 ×64 mm^2, 2 mm thickness)[47]. Electrical contact between the anode catalyst layer of the ½ MEA and the mixed-metal anode of the ElyFlow cell was established by the slightly increased pressure in the catholyte compartment (see Figure S3) and with a set of seven circular pieces of titanium expanded metal (GAB Titan, ASTM B265 Gr. 1, mesh size 0.5 ×0.5 ×4×2 mm, 35 mm diameter) fitted in the analyte compartment on the anode side. Titanium fleece (Bekaert, CURRENTO® 2GDL10N-0.25) was placed on each side of the expanded metal. The working electrode holder exposed an area of 10 cm^2 of the gas diffusion electrode to the electrolyte. Silicone gaskets between the compartments were used for sealing[48]. Further details regarding the cell configuration can be obtained from the ElyFlow manual[46]. CO_2 was supplied to the cell as a separate humidified gas stream at a flow rate of 100 ml•min^{-1} using Bronkhorst EL-FLOW controllers. A Perma Pure tube-in-shell humidifier (Perma Pure LLC, MH-110–12P-4) was used for the humidification of the gaseous CO_2, reaching up to 98% relative humidity[49]. The ultrapure water for the humidification was circulated with a polypropylene (PP) membrane pump (Gaskatel GmbH, 83721). The membrane pump for the catholyte circulation was controlled by a commercial control box (Gaskatel GmbH, Control box GCB-TT, 83800), which was also used to display the temperature measured in the catholyte vessel with a Pt100 sensor (Gaskatel GmbH, 83911). The pressure control system was used to adjust the differential pressure across the GDE, $\Delta p_{GDE,}$ and maintain flow-by conditions. The pressure on the CO_2 gas side was directly controlled, whereas the catholyte pressure was only measured. Correspondingly, the CO_2 pressure was set to maintain Δp_{GDE}~0 mbar during operation (see Figure S3 in the supporting information). Gas analysis was conducted with a gas chromatography system (GC) (Thermo Scientific Trace 1310). The gas outlet of the flow cell was connected to the headspace of the catholyte vessel to allow for the separation of droplets that are carried in the gas stream. Consequently, the composition of the gas from the catholyte gap and from the cathode gas outlet was measured as one single flow. Before the gas entered the gas chromatograph, it was dried in a membrane-based dryer (Perma Pure LLC, PD-50T-12MPP). The gas flux was measured with a drum-type gas meter (Ritter, TG0.5/6, 1 l•h^{-1} to 60 l•h^{-1}).

2.4. Flow cell experiments

The flow cell experiments were conducted at ambient temperature without external heating (see Table S5) and with 400 ml 2 M $KHCO_3$ catholyte. The cell was assembled and tightened with a stepwise increase of torque from 1.0 to 2.0 to 3.0 Nm. A reversible hydrogen electrode (RHE) (Mini Hydrogen Reference Electrode Mini-HydroFlex, Gaskatel GmbH, 81020) was used as a reference electrode and the reference electrode chamber was filled with catholyte before starting the experiment. To start up the cell, the CO_2 gas flow rate was set to 100 ml•min^{-1}, the water circulation for the humidification was started, and the Ar flow rate for the dryer was set to 200 ml•min^{-1}. Next, the CO_2 pressure was set to 90–100 mbar, and the catholyte flow rate was slowly increased to ~30 ml•min^{-1} such that the differential pressure equilibrated. A VSP-300 potentiostat (Biologic) equipped with a 2 A/30 V booster card was used for the flow cell experiments. The potentiostat cables were connected with the cell (working/sense on working electrode, reference electrode, and working/sense on counter electrode), and the measurement protocol shown in Figure S4 was started. Once the electrolysis started, the pressure on the gas side was increased to maintain Δp_{GDE}~0 mbar. At the end of the experiment, the GDE was removed from the cell, washed with ultrapure water three times, and placed in a fumehood to dry overnight. The cell and the lines were cleaned by circulating ultrapure water three times. The sealings were cleaned separately first with ethanol and then with ultrapure water.

The Faradaic efficiency FE(i) of species i was calculated with Eq. (1):

$$FE(i) = \frac{\dot{V}_{tot} \cdot x_i \cdot z \bullet F}{V_m \cdot I} \quad (1)$$

Where $\dot{V}_{tot}$ is the gas flux exiting the cell from the catholyte and cathode gas compartment measured with the Ritter gas meter, x_i is the molar fraction of component i in the gas stream measured with the GC, V_m is

the molar volume at standard conditions (24.46 l•mol^{-1}, 25 °C, 1 atm), z is the number of electrons transferred in the reaction (z = 2 for CO & H_2), I is the current (2 A in the galvanostatic experiments) and F is Faraday's constant (F = 96485 C•mol^{-1})[50].

2.5. Pristine and post-test electrode characterization

2.5.1. Determination of the electrochemically active surface area (ECSA)

GDE samples were cut into pieces of 20 × 20 mm size using a manual hydraulic press STAR MA3 (Lucris Manufacturing) and stored at ambient conditions before use. All experiments were performed at ambient conditions in a 1 M $KHCO_3$ electrolyte solution (Fisher Scientific, 450640050, p.a.) in a three-electrode configuration using an in-house developed electrochemical cell[51] connected to a SP-300 potentiostat (Biologic). The setup is referred to in the main text as the "CV setup". The GDE sample was connected as the working electrode, a Pt wire (23 cm, ALS) served as the counter electrode, and a RHE (Gaskatel GmbH) was used as the reference electrode. The geometric surface area of the GDE exposed to the electrolyte solution was A_{geo} = 0.28 cm^2. After cell assembly, the sample was equilibrated at OCP for 10 min. A constant potential of 0.7 V vs. RHE was applied for 30 s to stabilize the sample current before performing cyclic voltammetry (CV) measurements to analyze the double-layer capacitance (C_{dl}). CV curves were recorded between 0.7 and 0.8 V vs. RHE at varying scan rates from 200 mV•s^{-1} to 10 mV•s^{-1} for 10 cycles each (200, 150, 100, 75, 50, and 25 mV•s^{-1}) or 5 cycles (10 mV•s^{-1}). The average current of the anodic and the cathodic sweep at 0.75 V vs. RHE of the final cycle was plotted versus the scan rate to determine the double-layer capacitance from the slope of the linear fit.

2.5.2. Laser scanning microscopy

Laser scanning microscopy (LSM) images and height profiles of 5 randomly selected areas of each GDE were acquired with an Olympus Lext OLS4100 microscope using a 10x magnification lens (field of view: 1.28 ×1.28 mm). For the calculation of the roughness parameters, only areas without cracks in the microporous layer (MPL) were considered, as shown in Figure S27. Furthermore, the noise filter and tilt adjustment were applied before the calculation.

2.5.3. Contact angle measurement

The contact angles of the pristine and used GDEs were measured with a dataphysics OCA 200 device, using 4 µl droplets of 2 M $KHCO_3$ with a dosing speed of 1 µl•s^{-1}. The SCA20® software was used for analysis, and the contact angle of at least 10 droplets was averaged. A 500 µl gastight syringe (Hamilton) was used, and the pristine and used GDE samples were cut into thin strips for analysis using ceramic scissors. An increased droplet volume of 8 µl was used for the contact angle measurement of the uncoated Sigracet 36BB GDL, due to the low adhesion.

2.5.4. Scanning electron microscopy & energy-dispersive X-ray spectroscopy

Scanning electron microscopy (SEM) images were acquired using a FEI Quanta FEG650 microscope at 10 mm working distance, 20 kV, and spot size 3.0. Energy dispersive X-ray spectroscopy (EDS) was used to evaluate the distribution of PTFE on the GDE. For EDS mapping, an Octane elite detector (Ametek EDAX) and the Apex EDS software were used. The spot size was increased to 5.5, the acceleration voltage decreased to 10 kV and the working distance was kept at 10 mm. The resolution was set to 1024 × 800, the dwell time to 50 µs and the number of total frames to 64.

2.5.5. Porometry

Through-pore size distributions were measured using a Quantachrome Porometer 3 G applying the full pore size analysis method (wet then dry). The GDE/GDL samples were cut into circles of 18 mm in diameter to fit into the sample holder (1.33 cm^2) and wetted with Quantachrome Porofil (1.85 g•ml^{-1}, 16.0 dyn•cm^{-1}) for at least 1 min before starting the measurement. The pore size was measured in the range from 100 µm to 9 µm (corresponding to a 6.40 mbar to 70.46 mbar pressure range).

3. Results and discussion

To investigate the role of the binding agent, silver-based GDEs were prepared by ultrasonic spray coating of silver nanoparticle inks with the binding agents shown in Figure S1 onto Sigracet 36BB GDLs (catalyst+binding agent loading ~1.85 mg•cm^{-2}, binding agent content ~8.5 wt% with respect to the catalyst mass, see Table S2 and Table S3). Furthermore, a GDE was prepared with an ink containing only Ag nanoparticles and no binding agent. In Fig. 1, selected examples of SEM images of the Fumion-based GDE illustrate the electrode design: A thin catalyst layer consisting of silver nanoparticles on top of the carbon-based Sigracet 36BB GDL (also see Figure S58), which exhibits ~20–30 µm wide cracks, which were already present in the as-received GDL substrates.

In order to account for the mismatch between the ink and the catalyst layer composition occurring with ink-based methods, the respective deposition efficiencies for the binding agents and the silver nanoparticles were determined by spraying them individually (see Table S1) [41,52–54]. Aside from the GDE prepared with PTFE as the binding agent, the electrodes were used without further heat treatment. In Table 2, the ionic conductivity, the water uptake, and the ion exchange capacity of the investigated binding agents are listed.

3.1. Heat treatment of PTFE gas diffusion electrodes

The PTFE gas diffusion electrodes were heat-treated at 250 °C for 2 h in an Ar atmosphere according to the methodology reported by Nwabara et al., with the motivation of homogenously distributing the PTFE particles across the catalyst layer as the particles are dispersed and not dissolved in the catalyst ink[35]. The heat-treatment did not lead to any mass losses (Table S4). The SEM micrographs and EDS maps in Figure S7 in the supporting information show that the heat-treatment did not lead to a homogeneous film formation of PTFE, as the micrometer-sized particles remain visible also in the heat-treated sample. Instead, the main effect was the observed sintering of the silver nanoparticles. This is in accordance with the sintering temperature of silver nanoparticles in the range of 200–300 °C [67–70], the melting temperature range of PTFE of 327–342 °C[71], and electrode preparation methodologies in which PTFE is sintered at about 330–340 °C [72,73]. To further evaluate the effect of the heat-treatment, the non-heat-treated PTFE-based GDE, as well as a heat-treated GDE without binding agent, were used in flow electrolysis tests and analyzed via contact angle measurement, EIS, CV, LSM and SEM (see Figure S9, Figure S10, and Figure S11).

3.2. Electrochemical characterization

The prepared gas diffusion electrodes were characterized via EIS and CV to evaluate the double-layer capacitance and thus the relative ECSA. Fig. 2**a** shows the impedance spectra for the pristine GDEs, which were obtained from measurements in the flow cell and fitted based on the equivalent circuit model shown as an inlay. One semicircle was observed for all GDEs, which was corroborated by the distribution of relaxation time (DRT) analysis as given in Figure S14 and Figure S15. The presence of smaller peaks and shoulders in the DRT spectra of certain anion-conducting ionomers (Aemion, Fumion, Sustainion) was observed, which was interpreted as a consequence of noise in the corresponding EIS spectra. On the other hand, the peaks could indicate ion and mass transport processes as reported in a study on a copper electrocatalyst investigated with DRT analysis[74].

While the high-frequency resistance R_0 was independent of the binding agent, the charge-transfer resistance R_{ct} was strongly dependent

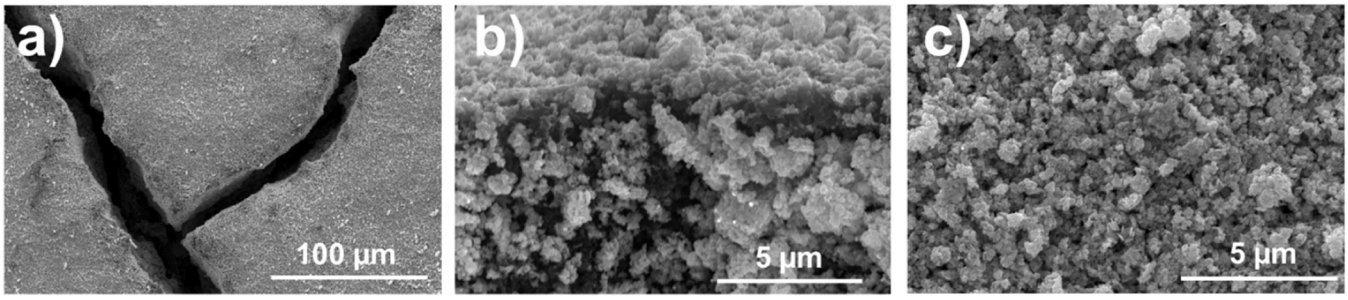

Fig. 1. (a) Top-view SEM image of the Fumion-based GDE. The cracks of the Sigracet 36BB gas diffusion layer are clearly visible. (b) Cross section view along a GDL crack, showing silver nanoparticle deposition also on the crack walls. (c) Top-view SEM image of the catalyst layer showing silver nanoparticles.

Table 2
Physicochemical properties of the investigated ionomers/binding agents reported in the literature: Ionic conductivity, water uptake, ion exchange capacity and swelling ratio.

Ionomer/binding agent	Ionic conductivity (25 °C, mS•cm^{-1})	Water uptake (%)	Ion exchange capacity (meq/g)
Fumion FAA-3	8.22 (OH^-)[55]	19 (30 °C)[56]	1.7–2.2[55]
Sustainion XA-9	64 (OH^-)[55]	80 [55,57]	1.1[55]
PiperION	60–80 (OH^-) [55]	30–60, 50 (30 °C) [58,59]	2.3–3.5[55]
Nafion D520	100 (H^+)[60][a]	27 (30 °C)[61]	1.03 –1.12[62]
Aquivion D72–25BS	100 (H^+)[60][b]	40 (30 °C)[61]	1.35–1.43[63]
Aemion+ AP3-HNN9	4–9 (Cl^-)[55]	20–50 (80 °C) [64]	1.9–2.7[64]

[a] For Nafion D520 (>1000 EW) we consider the conductivity of a N112 (1100 EW) membrane immersed in water. [b] For Aquivion D72–25BS we assume the same ionic conductivity as for Nafion D520. Due to the higher water uptake a higher conductivity would be expected [65,66].

on the binding agent present in the ink. Overall, the presence of a binding agent in the ink resulted in a higher charge-transfer resistance compared with the GDE prepared without binding agent. For instance, the GDE prepared without binding agent exhibited an R_{ct} of ~5 Ω, whereas an increased charge-transfer resistance in the range of ~7.5 Ω was observed for the Fumion GDE. Qualitatively, this observation was in accordance with the lower ionic conductivity of the ionomers compared to the bulk electrolyte (2 M $KHCO_3$). As Fig. 2**b** illustrates, the observed charge-transfer resistance correlates with the ionic conductivity of the binding agent. To ensure comparability, only samples prepared without heat treatment and using ethanol as the ink solvent are considered. The correlation for all samples is shown in Figure S20. Even when considering thick ionomer films (11 wt% Nafion in 3 mg•cm^{-2} IrOx catalyst layer prepared by ultrasonic spray coating: 100–300 nm with agglomerates up to 400 nm[76]), it seems unlikely that the observed increase in R_{ct} is caused solely by the lower ionic conductivity of the ionomer phase compared to the bulk $KHCO_3$ electrolyte (increase of ionic conductivity from 5 to 100 mS•cm^{-1} with ionomer thickness of 400 nm would decrease R_{ct} of a planar electrode from 8 mΩ•cm^2 to 0.4 mΩ•cm^2). However, the ionomer can account for a significant volume fraction in the catalyst layer considering its lower density compared to silver metal and the water uptake[77]. When discussing the effect on the overall cross-plane conductivity, it seems more likely that the network formed by the ionomer across the whole catalyst layer must be considered[78]. In addition to the intrinsic ionic conductivity, effects on the microenvironment, like the local CO_2/H_2O ratio and CO_2 solubility in the wet ionomer phase, could play a significant role in dictating the charge-transfer resistance in CO_2 electroreduction [17,25,28]. The observed changes of R_{ct} in the order of ~3 Ω correspond to changes of the area-specific resistance of ~30 Ω•cm^2, which is comparable to experimental findings obtained by Nwabara et al[35].

In Fig. 2**c,** the current measured in CV scans is shown as a function of the scan rate for the GDEs prepared with different binding agents. The choice of the binding agent can significantly affect the double-layer capacitance of the GDEs, with a range from 0.55 mF•cm^{-2} for the PTFE-based GDE up to 3.54 mF•cm^{-2} for the PiperION-based GDE, respectively. However, it should be noted that due to the heat treatment applied to the PTFE-based samples and the different ink solvent used for the Aemion-based samples (ethanol/acetone instead of ethanol), the effects of these binding agents were superimposed on those arising from the respective preparation methodologies. The CV scans are given in the supporting information in Figure S17 and Figure S18, next to the data in Table S10. As an example, CV scans and data analysis for the Nafion-based GDE are shown in Fig. 3. According to Eq. 2, C_{dl} is directly correlated to the accessible electrochemically active surface area (ECSA). C_s corresponds to the specific capacitance of an atomically smooth planar surface of the catalyst material. A C_s of 20 mF•cm^{-2} was adopted based on typically reported values at a smooth silver/electrolyte interface [79,80]. Accordingly, the ECSA data reported in Table S10 should be only used for relative comparison.

$$ECSA = \frac{C_{dl}}{C_s} \quad (2)$$

To obtain C_{dl}, CV measurements were carried out at multiple scan rates v in a potential range within which the measured current is expected to be due to double layer charging (silver nanoparticle oxidation is reported at +0.4 V vs. Hg/HgO in 0.1 M phosphate buffer, pH 7, equivalent to +0.9 V vs. RHE)[81]. A nearly rectangular shape of the CV curve (Fig. 3**a**) indicated that the measured current arises from the charging and discharging behavior of the electrical double layer[82]. For strong resistive behavior of the catalyst layer, however, the CV curves become distorted at high scan rates. According to Eq. 3, C_{dl} corresponds to the slope of the linear fit of the measured current I vs. the scan rate v.

$$I = v \cdot C_{dl} \quad (3)$$

As shown in Fig. 3**b**, a linear relation between the scan rate and the current response was observed for $v \leq 100$ mV•s^{-1}. For $v > 100$ mV•s^{-1}, this linear relation starts to disappear, which could be due to the mass transport limitation (ion penetration in the bulk of the catalyst layer, transport of product from the catalyst to the electrolyte solution) at a fast acquisition time, leading to a reduction of the measured current. For this reason, only the current response for scan rates of up to 100 mV•s^{-1} was considered to determine C_{dl}.

The capacitance values determined by CV are comparable to data reported on silver-based GDEs by Yu et al. in the range of 0.5–1.9 mF•cm^{-2}. While for the PiperION-based GDE (1.9 mF•cm^{-2}) and the Nafion-based GDE (1.4 mF•cm^{-2}), the same qualitative trend was reported, the capacitance of the Sustainion-based GDE (0.5 mF•cm^{-2}) was reported to be lower than the reference sample without a binding agent (0.9 mF•cm^{-2}). The procurement of the ionomers from

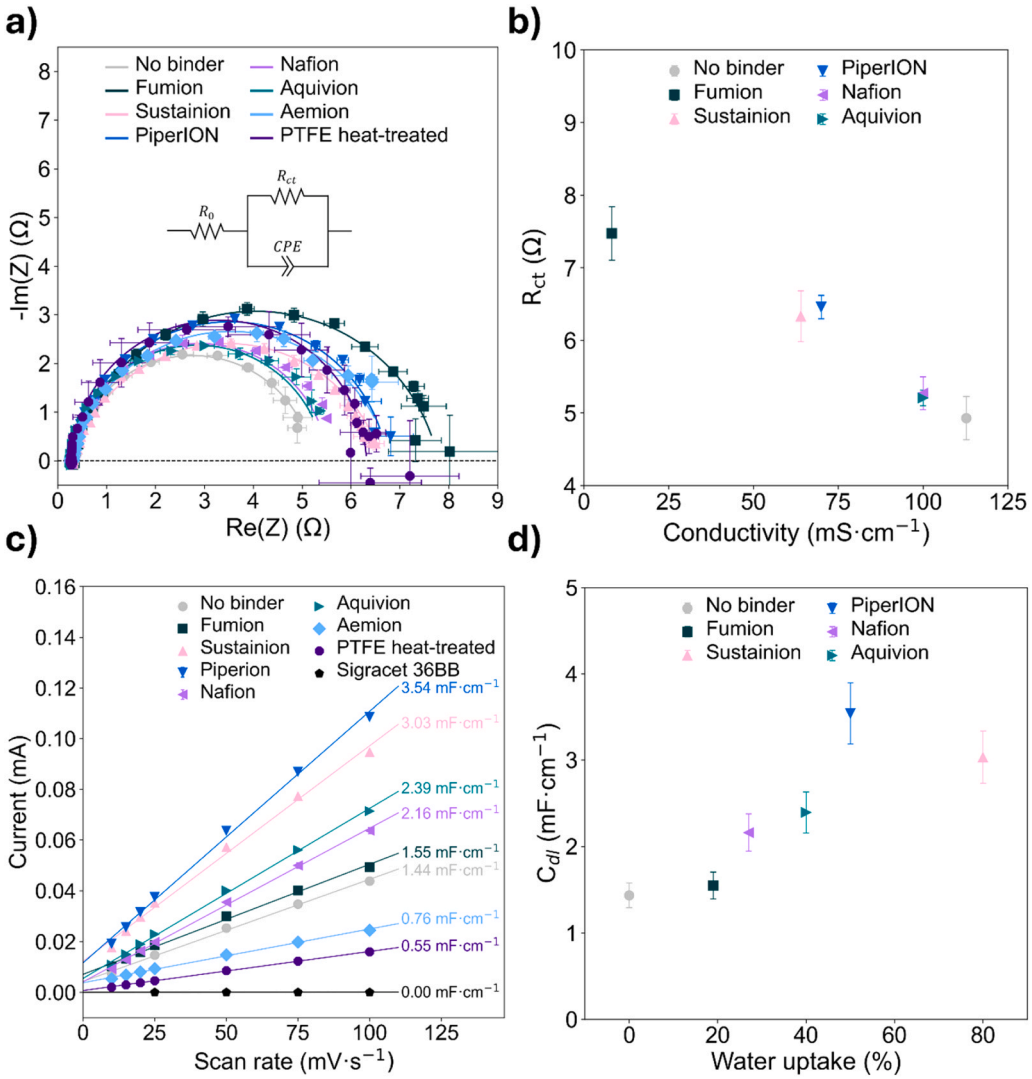

Fig. 2. (a) Electrochemical impedance spectra of the silver-based GDEs with different binding agents at −10 mA in the frequency range from 100 kHz to 100 mHz with 7 points per decade including the fit based on the shown equivalent circuit model. Measurements were performed in the flow cell and averaged from three individual measurements. The error bars show the standard deviation. (b) Fitted charge transfer resistance R_{ct} as a function of the ionic conductivity of the binding agent used in the fabrication of the respective GDE as given in Table 2. Only the samples prepared with ethanol as ink solvent and without heat treatment are shown for comparability. In case of the GDE without binder the conductivity of the bulk electrolyte (2 M $KHCO_3$) was considered, which was interpolated from experimental data as given in Fig. S2[75]. (c) Double-layer capacitance of the GDEs estimated from the slope of current vs. scan rate plots obtained from CV measurements in the CV setup[51] (see Fig. S17). (d) Fitted double-layer capacitance C_{dl} as a function of the water uptake of the binding agent used in the fabrication of the respective GDE as given in Table 2. For the sample prepared without a binder we assume a water uptake of zero. Only the samples prepared with ethanol as the ink solvent and without heat treatment are shown for comparability reasons. An estimated error of 15% is shown by error bars.

different suppliers might explain the inconsistency [27].

Fig. 2**d** shows a positive correlation between the double-layer capacitance of the GDE samples obtained from the CV measurements and the water uptake of the ionomer applied as the binding agent in the respective samples as reported in Table 2. To ensure comparability, only samples prepared without heat treatment and ethanol as the ink solvent are considered. The correlation for all samples is shown in Figure S19. Overall, the ionomer addition increased the double-layer capacitance compared with the GDE prepared without a binding agent. A clear increase in capacitance was observed for ionomers with higher water uptake: Fumion, with a water uptake of 19%, exhibited a capacitance of only 1.55 mF•cm^{-2}, whereas PiperION and Sustainion, which exhibited the highest water uptakes among the investigated ionomers (approximately 50% and 80%, respectively), showed substantially higher capacitances of 3.54 mF•cm^{-2} and 3.03 mF•cm^{-2}, respectively. These results are consistent with the hypothesis that the ionomer forms an interconnected network within which the nanoparticles are embedded, thereby increasing the fraction of the silver nanoparticle surface that is electrochemically accessible through the ionomer/electrolyte phase, rather than merely forming an external coating around the nanoparticles.

There were deviations between the double-layer capacitance by CV and EIS given in Figure S21 in the Supporting Information. The discrepancy may have arisen from the different time scales employed by the two techniques, as potential-induced rearrangements of the interfacial charge distribution can exhibit characteristic relaxation times and consequently contribute differently to the capacitance determined by cyclic voltammetry and EIS[83].

3.3. *Flow electrolysis experiments*

Fig. 4 shows the transient evolution of the Faradaic efficiency (FE) for hydrogen and carbon monoxide formation during 2 h galvanostatic electrolysis experiments in the flow cell setup at −200 mA•cm^{-2}. The FE

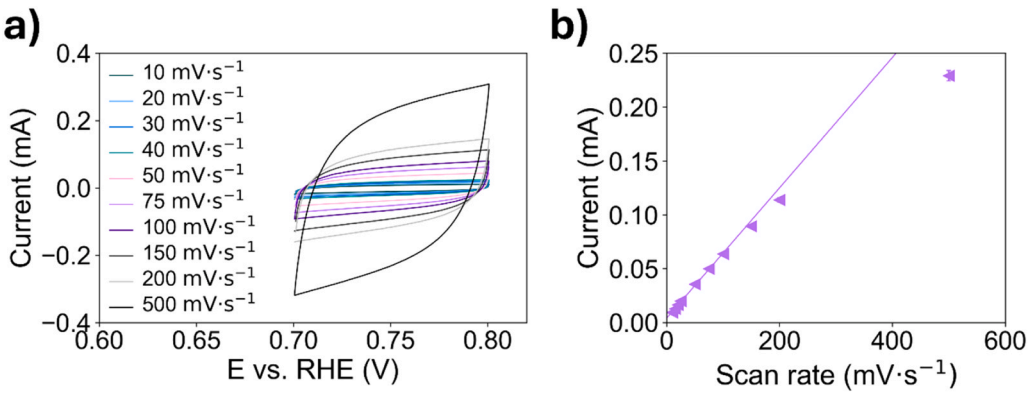

Fig. 3. Analysis of the double-layer capacitance C_{dl} in 1 M $KHCO_3$ for the GDE with Nafion binder. (a) CV curves in the non-Faradaic region at 500–10 mV•s^{-1} scan rate vs. RHE. (b) Relationship between capacitive current and scan rate. The capacitive current corresponds to the average of the anodic and cathodic sweep at 0.75 V vs. RHE obtained in CV measurements between 0.7 V and 0.8 V vs. RHE.

(H_2) ranged between 1% and 4% in the first 10 min for all GDEs except for the PiperION-based one and rose up to 22% for the Sustainion-based GDE and 38% for the PiperION-based GDE at the end of the electrolysis experiment. In general, a slight increase of the FE(H_2) was observed for all GDEs. Compared to the other GDEs, the PiperION-based GDE exhibited an increased FE(H_2) of ca. 26% in the first 10 min of the electrolysis experiment. The Sustainion- and PiperION-based GDEs performed less favorably compared to the GDEs prepared with Nafion and no binding agent, which both yielded 16% FE(H_2) after 2 h. The other GDEs prepared with Fumion, Aemion, Aquivion, or PTFE exhibited a decreased FE(H_2) in the range of 9–11%. The sum of FE(H_2) and FE (CO) was close to 100% indicating that side reactions such as formic acid formation were not significant. This observation is supported for the most part by other studies employing different binding agents in catholyte gap electrolysis setups. For instance, in a recent study comparing Nafion, Sustainion, and PTFE a more favorable performance for Nafion and PTFE (~100% FE(CO) and 105 −110% FE(CO) respectively) than for Sustainion (decrease from~95% to ~80% FE(CO)) was reported in the first 2 h of a 6 h experiment[35]. In another study, Nafion-, Sustainion-, and PiperION-based GDEs were prepared with PTFE nanoparticles. While the FE(H_2) for Nafion and Sustainion was negligible, the PiperION-based GDE produced a significant amount of hydrogen (FE (H_2)~15%) at −150 mA•cm^{-2}[27].

The cathode potentials are given in Figure S22 and Figure S23 in the Supporting Information and revealed only minor effects of the binding agent. As shown in Figure S24 in the supporting information, the potential during the −200 mA•cm^{-2} electrolysis did not correlate with the ionic conductivity of the ionomer that was applied in the fabrication of the GDEs, in contrast to the correlation of R_{ct} and ionic conductivity that was found at low current density (−1 mA•cm^{-2}) in the impedance spectra (see Fig. 2**b**). This could underline the mass transfer limitation of CO_2 at the higher current density of −200 mA•cm^{-2} and might indicate that the ionomer can significantly affect the availability of CO_2 at the catalyst layer and the diffusion pathways to it at higher current densities [22,25,84,85].

3.4. Wetting properties

Fig. 5 shows the initial contact angle of electrolyte droplets (2 M $KHCO_3$) on the pristine and used GDE surfaces. Apart from the PiperION-based GDE, which exhibited a more hydrophilic surface with a contact angle of 82 ± 7°, and the Aemion-based GDE with a contact angle of 111 ± 3°, the other binding agents did not affect the hydrophobicity significantly, with the contact angles being in the range of 132–144°. The contact angles of all coated GDEs decreased in comparison to the contact angle of the uncoated Sigracet 36BB GDL (MPL side, see Figure S25) of 149 ± 2°, which is most likely due to the hydrophilicity of the silver nanoparticles[86]. For the Fumion-, Sustainion- and PTFE-based GDE as well as the GDE prepared without a binding agent, the contact angles were between 130° and 140°. Applying the fluorinated compounds Nafion and Aquivion increased the contact angle up to 144° and 141°, respectively. Recent wetting data reported for silver-based GDEs with Nafion (149 ± 2°), Fumion (138 ± 6°), and PTFE as a binding agent (150 ± 2°) mainly support the findings in this study. Sigracet 28BC carbon paper (same 5 wt% PTFE content as Sigracet 36BB) and a similar loading (~1 mg•cm^{-2}), as well as ionomer content (~10 wt% of catalyst amount), was applied[36]. The discrepancy with respect to the PTFE-based GDE can be explained by two factors: The heat-treatment (not conducted in the referenced study) and a different dispersion type and supplier. Despite the agreement with respect to the contact angle data corresponding to the pristine GDEs, a significant deviation was found with respect to the wetting data of the used GDEs (after 3 h electrolysis at 4 V cell voltage, initial current density ~ −50 mA•cm^{-2}, decreasing over time), with contact angles reported to be below 100°. This discrepancy most likely is caused by remaining $KHCO_3$ precipitates on the catalyst layer, which increase the hydrophilicity of the surface[87].

3.5. Catalyst layer stability

Fig. 6**a** and **b** depict LSM images of pristine and operated GDEs prepared with Nafion and Sustainion, respectively, at tenfold magnification. The Sustainion-based GDE exhibited pronounced catalyst detachment in the form of flakes, exposing the underlying MPL (black). In contrast, the Nafion-based catalyst layer showed substantially less flaking, with no apparent areas of catalyst detachment. The observed catalyst loss may also contribute to the darkening of the catalyst layer after electrolysis, as observed in the photographs in Figure S8 in the Supporting Information.

Fig. 6**c** compares the root mean square surface roughness (Sq) of the pristine and operated catalyst layers prepared with Nafion and Sustainion. In the pristine state, the catalyst layers exhibited similar surface roughness values of 2.0 ± 0.8 µm and 1.8 ± 0.7 µm for the Nafion- and Sustainion-based GDEs, respectively. After electrolysis, the surface roughness of the Nafion-based catalyst layer remained largely unchanged at 2.2 ± 0.8 µm, whereas that of the Sustainion-based catalyst layer increased substantially to 4.8 ± 2.5 µm. The increase in Sq is consistent with the pronounced catalyst layer flaking observed in the corresponding LSM images. The relatively large deviations in Sq compared with the absolute roughness values most likely result from substantial spatial variations in surface morphology between different areas of the catalyst layer.

The pronounced catalyst detachment and associated increase in surface roughness indicate that the ionomer can play an important role

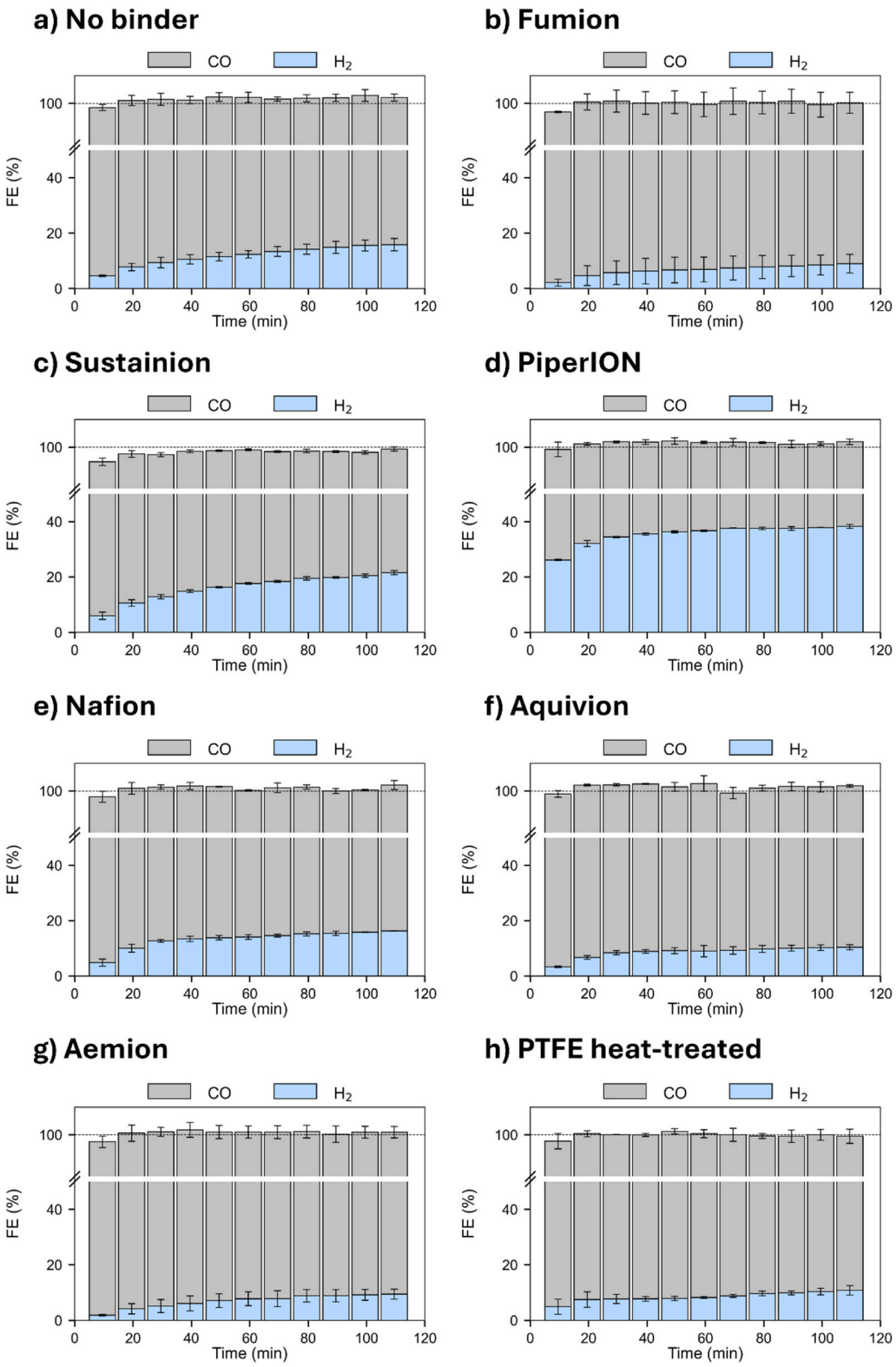

Fig. 4. Faradaic efficiency (FE) for carbon monoxide (CO) and hydrogen (H_2) formation in the 2 h galvanostatic experiment performed in the flow cell at a current density of 200 mA•cm^{-2}. The electrolysis experiments were performed at room temperature (~25 °C) with a temperature increase of ~15 °C during the experiment (see Table S5) and with flowing 2 M $KHCO_3$ as the catholyte and a geometric electrode area of 10 cm^2.

in the mechanical stabilization of the catalyst layer. Insufficient mechanical cohesion within the catalyst layer may facilitate catalyst detachment during electrolysis. In addition, electrolyte flow as well as the formation and detachment of gas bubbles may impose mechanical stresses on the catalyst layer and thereby accelerate catalyst loss [88, 89]. However, the present comparison is not intended to constitute a direct benchmark of the investigated ionomers, since their contents in the catalyst layers were not individually optimized. Rather, these results demonstrate that the choice of ionomer and its interaction with the catalyst layer can substantially affect the mechanical stability of the

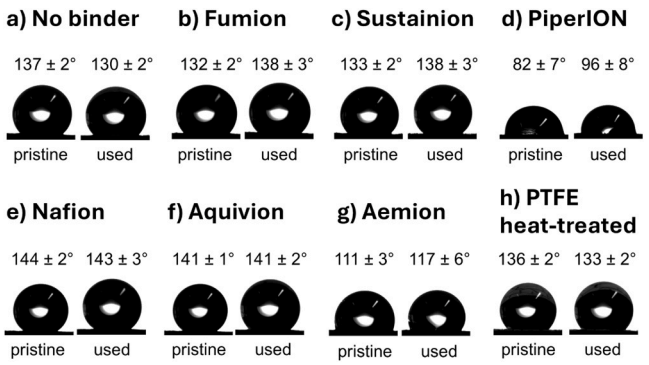

Fig. 5. Initial contact angle of 2 M $KHCO_3$ droplets on the pristine and used gas diffusion electrode surface prepared with the different binding agents. The used GDEs were washed with ultrapure water.

resulting GDE.

Additional LSM data are provided in the Supporting Information, including the complete surface roughness data in Figure S28, and LSM images of pristine and operated GDEs prepared with the other binding agents in Figure S30. Catalyst layer detachment was also reflected in the electrochemical impedance spectra, as demonstrated by the comparison of pristine and operated GDEs in Figure S26. Furthermore, SEM images of the pristine and operated catalyst layers (Figure S38 to Figure S57) provide additional evidence of catalyst detachment and support the LSM observations. Qualitatively, similar catalyst layer detachment behavior was previously reported as indicated through SEM images by Gonugunta et al. [36,41].

For the GDE prepared without a binding agent, the particles forming the catalyst layer appeared to increase in size after operation, as shown in Figure S38 and Figure S39. A similar increase in particle size was previously reported in the literature[38].

3.6. The role of the ionomer with respect to hydrogen evolution

Fig. 7 provides a visual representation of the correlation between the Faradaic efficiency for hydrogen formation, $FE(H_2)$, and the ionomer water uptake, as well as the contact angle of the pristine GDEs. The data shown in Fig. 7**a** indicates a positive correlation between the $FE(H_2)$ and the water uptake of the ionomer. A higher water uptake might lead to a lower CO_2/H_2O-ratio, which would increase $FE(H_2)$ in accordance with the experimental findings[17]. A similar trend was reported by Kim et al., who synthesized polycarbazole-based anion-exchange ionomers with different functional groups for silver-based CO_2 electroreduction, including trimethyl phosphonium (TMP)-, tetramethyl imidazolium (tmIM)-, and 1,4-diazabicyclo[2.2.2]octane (DABCO)-groups[28]. The water uptake of these ionomers increased in the order of TMP (~55%), tmIM (~75%), and DABCO (~95%). The H_2 current density in an H-cell at the maximum investigated potential (IR-corrected) of −1.1 V vs. RHE increased in the same order from ca. $-0\ mA{\bullet}cm^{-2}$ (TMP), ca. $-1\ mA{\bullet}cm^{-2}$ (tmIM), to $-4.5\ mA{\bullet}cm^{-2}$ (DABCO).

As discussed in Section 3.4, apart from PiperION and Aemion, the different binding agents did not significantly affect the hydrophobicity of the catalyst layer, as shown in Fig. 7**b**. Correspondingly, we found that the initial product distribution obtained with the GDEs based on these binding agents was rather similar (~10% $FE(H_2)$ at 10–20 min). By contrast, the more hydrophilic PiperION-based GDE (82° contact angle) exhibited a significantly increased $FE(H_2)$ of > 30% in the initial phase of the electrolysis experiment (10–20 min). Within this argumentation, the Aemion-based GDE must be seen as an outlier that produced a relatively small amount of hydrogen despite its reduced hydrophobicity (111° contact angle compared to 130–140°). Nonetheless, the finding that hydrophobic GDEs exhibit decreased $FE(H_2)$ is still valid [27,40].

Furthermore, the through-pore size distribution of the GDEs was

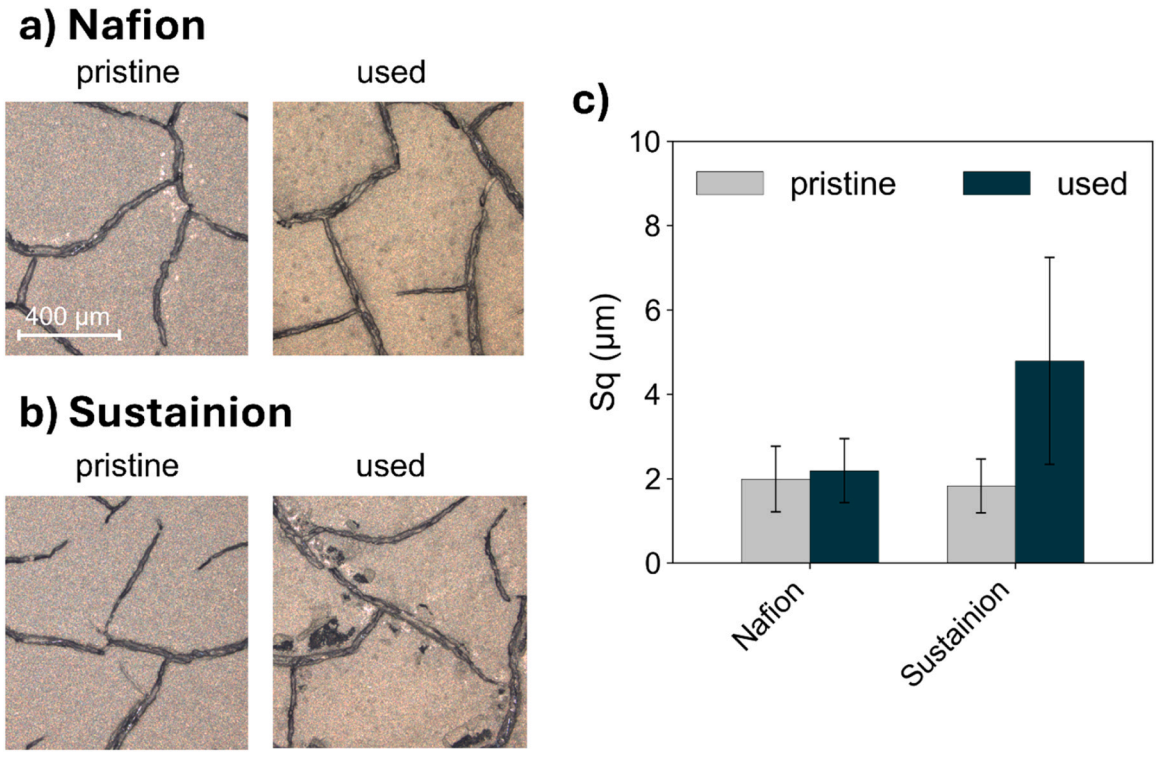

Fig. 6. Laser scanning microscopy images at 10x magnification of the pristine and used catalyst layers of the GDEs prepared with Nafion (a) and Sustainion (b). Scale bar (top left) valid for all images. (c) Root mean square surface roughness (Sq) of the pristine and used catalyst layers of the GDEs prepared with Nafion and Sustainion. The increase in surface roughness correlates with the flaking-off of the catalyst layer. Only areas without cracks of the MPL (Sigracet 36BB) were considered for the data evaluation (see Fig. S27).

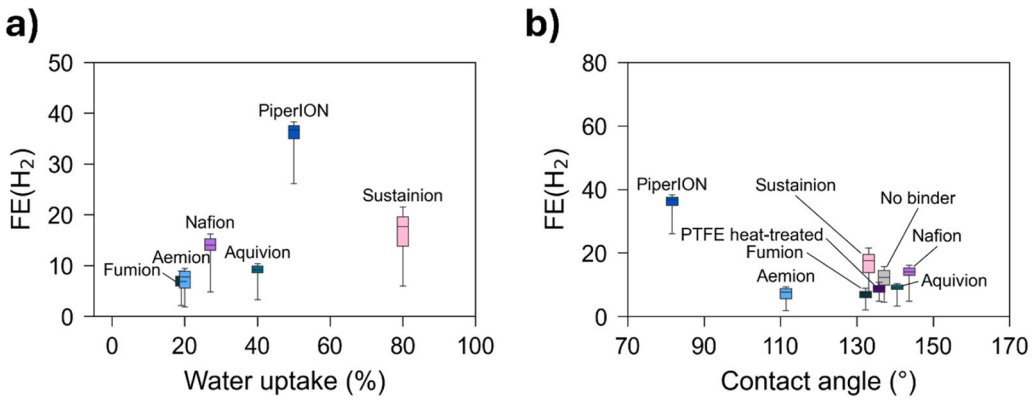

Fig. 7. Faradaic efficiency for hydrogen formation FE(H_2) as a function of the water uptake (for Aemion the lower-bound value in Table 2 of 20% was used due to the lower temperature in the experiments compared to the temperature given in the product sheet for the water uptake [64,90], which is in accordance with the low water uptake of an AF3-HWK9 membrane[64]) of the respective ionomers as given in Table 2 (a) and the initial contact angle of 2 M $KHCO_3$ droplets on the pristine GDE surface (b).

measured (see Figure S31 to Figure S35 in the supporting information), revealing no significant impact of the applied ionomer on the mean and shape of the distribution in comparison to the bare Sigracet 36BB GDL. In addition, no clear correlation can be observed between FE(H_2) and the ion exchange capacity of the ionomer as reported in Figure S36 in the Supporting Information.

For a deeper understanding of the role of the ionomer and its effect on the CO_2/H_2O-ratio, a comparative determination of important transport properties like the solubility and permeability of CO_2 in thin ionomer films under in-situ conditions would be desirable, as the data is usually reported only for one or two ionomers under the same conditions [28,91–94].

4. Conclusions

In this study, the most frequently used binding agents for the silver-based low-temperature electroreduction of CO_2 to CO were employed to prepare gas diffusion electrodes via ultrasonic spray coating to elucidate the role of the binder in the electroreduction process. The key findings of the study are summarized as follows:

1. Charge-transfer resistance: Electrochemical impedance spectroscopy, conducted at a low current density of -1 mA•cm^{-2}, revealed a decrease in the charge-transfer resistance with increasing ionic conductivity of the ionomer. This finding highlights the importance of ionomer ionic conductivity for efficient ion transport within the catalyst layer and, consequently, for the electrochemical charge-transfer kinetics of the GDE.
2. Double-layer capacitance: The double-layer capacitance determined by cyclic voltammetry increased with the water uptake of the ionomer incorporated into the catalyst layer. Despite comparable silver loadings, the Sustainion- and PiperION-based GDEs exhibited substantially higher capacitances than the ionomer-free GDE. This behavior suggests that incorporation of highly water-uptaking ionomers increases the electrochemically accessible interfacial area, potentially through the formation of an ionomer network within the catalyst layer in which the silver nanoparticles are embedded.
3. Hydrogen Faradaic efficiency: The use of the hydrophilic ionomer PiperION resulted in a pronounced increase in the Faradaic efficiency for hydrogen, FE(H_2), whereas the other ionomers did not significantly affect the selectivity. In addition to the contact angle of the pristine GDEs, the FE(H_2) showed a positive correlation with the water uptake of the ionomer. These results indicate that the water-management properties of the ionomer can influence the competition between CO_2 reduction and the hydrogen evolution reaction.
4. Catalyst layer stability: Post-test LSM and SEM characterization, supported by EIS analysis, highlighted the influence of the ionomer on the catalyst layer stability. Pronounced catalyst detachment was observed for the Sustainion-based GDE, whereas the Nafion-based catalyst layer, as an example, remained largely intact over the duration of the flow-cell experiment, demonstrating that ionomer selection is an important consideration for maintaining catalyst layer integrity during operation.

Future studies should investigate whether the relationships identified here between ionomer properties and GDE performance extend to other CO_2RR products, particularly formic acid and multicarbon products. Such studies would help determine which ionomer effects are generally applicable to CO_2 electroreduction and which are specific to the catalyst and reaction pathway. Furthermore, future investigations should focus on the properties and morphology of ionomer films formed around the catalyst particles. In particular, experimentally determining the CO_2 transport properties of thin ionomer films, including CO_2 permeability and solubility, would provide valuable insights into the accessibility of CO_2 at the catalyst–ionomer interface. Combining these measurements with the water uptake and ionic conductivity of the ionomers could help establish how ionomer properties govern the local CO_2/H_2O ratio and ion transport within the catalyst layer, and consequently the competition between CO_2 reduction and the hydrogen evolution reaction. Finally, investigating changes in ionomer morphology and catalyst–ionomer interactions during electrolysis would be valuable for understanding the observed differences in catalyst layer stability.

CRediT authorship contribution statement

Simon Emken: Writing – original draft, Conceptualization, Data curation. **Kristina Froehlich:** Writing – review & editing, Investigation, Data curation. **Alexander Bauer:** Writing – review & editing, Conceptualization. **Eva Jodat:** Funding acquisition. **André Karl:** Writing – review & editing. **Rüdiger-A. Eichel:** Funding acquisition.

Funding

Project Power2ValueChemicals. Grant nr. 03SFK2S5C. Funded by the German Federal Ministry of Research, Technology and Space, BMFTR.

Declaration of Competing Interest

The authors declare that they have no known competing financial

interests or personal relationships that could have appeared to influence the work reported in this paper

Acknowledgements

The authors gratefully acknowledge the funding received from the German Federal Ministry of Research, Technology and Space, BMFTR, within the project Power2ValueChemicals, grant nr. 03SFK2S5C. S.E. deeply thanks Leon Sestan for the assistance with the LSM image acquisition and Markus Küven, Markus Schmühl, Heinz-Willi Firmenich, and Marcel Turiaux for their assistance with the mechanical work required for the cell periphery.

Appendix A. Supporting information

Supplementary data associated with this article can be found in the online version at doi:10.1016/j.jcou.2026.103561.

Data availability

The data that support the findings of this study will be made openly available upon publication in JülichData at https://doi.org/10.26165/JUELICH-DATA/20LSMQ.

References

[1] M. Tayyab, M. Dreis, D. Blaudszun, K. Pellumbi, U. Nzotcha, H. Tempel, M. Q. Masood, H. Weinrich, S. Stießel, K. j Puring, et al., Energy Environ. Sci. 18 (2025) 6854–6873.
[2] C. Chen, J.F. Khosrowabadi Kotyk, S.W. Sheehan, Chem 4 (2018) 2571–2586.
[3] I.E.L. Stephens, K. Chan, A. Bagger, S.W. Boettcher, J. Bonin, E. Boutin, A. K. Buckley, R. Buonsanti, E.R. Cave, X. Chang, et al., J. Phys. Energy 4 (2022) 42003.
[4] X. She, Y. Wang, H. Xu, S. Chi Edman Tsang, S. Ping Lau, Angew. Chem. Int. Ed. 61 (2022) e202211396.
[5] A. Somoza-Tornos, O.J. Guerra, A.M. Crow, W.A. Smith, B.-M. Hodge, iScience 24 (2021) 102813.
[6] R. Krause, D. Reinisch, C. Reller, H. Eckert, D. Hartmann, D. Taroata, K. Wiesner-Fleischer, A. Bulan, A. Lueken, G. Schmid, Chem. Ing. Tech. 92 (2020) 53–61.
[7] T. Haas, R. Krause, R. Weber, M. Demler, G. Schmid, Nat. Catal. 1 (2018) 32–39.
[8] B. Endrődi, E. Kecsenovity, A. Samu, T. Halmágyi, S. Rojas-Carbonell, L. Wang, Y. Yan, C. Janáky, Energy Environ. Sci. 13 (2020) 4098–4105.
[9] H. Lee, S. Kwon, N. Park, S.G. Cha, E. Lee, T.-H. Kong, J. Cha, Y. Kwon, JACS Au 4 (2024) 3383–3399.
[10] Z. Liu, R.I. Masel, Q. Chen, R. Kutz, H. Yang, K. Lewinski, M. Kaplun, S. Luopa, D. R. Lutz, J. CO2 Util. 15 (2016) 50–56.
[11] M. Quentmeier, B. Schmid, H. Tempel, H. Kungl, R.-A. Eichel, ACS Sustain. Chem. Eng. 11 (2023) 679–688.
[12] M. Quentmeier, B. Schmid, H. Tempel, R.-A. Eichel, ACS Sustain. Chem. Eng. 12 (2024) 3876–3885.
[13] R.I. Masel, Z. Liu, H. Yang, J.J. Kaczur, D. Carrillo, S. Ren, D. Salvatore, C. P. Berlinguette, Nat. Nanotechnol. 16 (2021) 118–128.
[14] B. Hecker, E. Robens, H.E. Valencia, A. Windmüller, F. Muench, M. Meledina, H. Tempel, H. Kungl, J. Mayer, R.-A. Eichel, J. Electrochem. Soc. 170 (2023) 96505.
[15] M. Wang, J. Chen, B. Hu, Y. Xiao, L. Chen, J. Chen, L. Wang, ChemElectroChem (2025) e202400665.
[16] M. Li, M.N. Idros, Y. Wu, T. Burdyny, S. Garg, X.S. Zhao, G. Wang, T.E. Rufford, J. Mater. Chem. A 9 (2021) 19369–19409.
[17] S. Lee, J. Seo, C. Kim, Curr. Opin. Electrochem. 46 (2024) 101490.
[18] K. von Foerster, S. Sanz, K. Dzięcioł, U. Nzotcha, B. Rutjens, B. Schmid, H. Tempel, R.-A. Eichel, Green. Chem. 28 (2026) 7993–8003.
[19] J.A. Abarca, G. Díaz-Sainz, I. Merino-Garcia, G. Beobide, J. Albo, A. Irabien, J. Environ. Chem. Eng. 11 (2023) 109724.
[20] Z. Xing, L. Hu, D.S. Ripatti, X. Hu, X. Feng, Nat. Commun. 12 (2021) 136.
[21] A. Reyes, R.P. Jansonius, B.A.W. Mowbray, Y. Cao, D.G. Wheeler, J. Chau, D. J. Dvorak, C.P. Berlinguette, ACS Energy Lett. 5 (2020) 1612–1618.
[22] X. Du, P. Zhang, G. Zhang, H. Gao, L. Zhang, M. Zhang, T. Wang, J. Gong, Natl. Sci. Rev. 11 (2024) nwad149.
[23] A.T. Bell, Natl. Sci. Rev. 11 (2024) nwad232.
[24] R. Hong, L. Xing, N. Wang, L. Meng, L. Du, S. Ye, ACS Energy Lett. 11 (2026) 1193–1207.
[25] Y. Chae, H. Kim, D.K. Lee, U. Lee, H.Da Won, Nano Energy 130 (2024) 110134.
[26] S. Ruan, G. Tang, Z. Zhang, Q. Zhang, Y. Wang, S. Xie, Chem. Sci. 17 (2026) 96–117.
[27] C. Yu, T. Lei, L. Xu, C. Jin, J. Yi, S. Liu, S. Lin, Y. Yang, H. Song, K. Wang, et al., J. Mater. Chem. A 12 (2024) 17181–17192.
[28] C. Kim, J.C. Bui, X. Luo, J.K. Cooper, A. Kusoglu, A.Z. Weber, A.T. Bell, Nat. Energy 6 (2021) 1026–1034.
[29] N.V. Galbicsek, A. Kormányos, G.F. Samu, M.M. Ayyub, T. Kotnik, S. Kovačič, C. Janáky, B. Endrődi, Energy Fuels 38 (2024) 22307–22314.
[30] K. Seteiz, J.N. Häberlein, P.A. Heizmann, L. Bohn, S. Vierrath, J. Disch, ACS Appl. Eng. Mater. 2 (2024) 1654–1662.
[31] J.A. Abarca, L. Warmuth, A. Rieder, A. Dutta, S. Vesztergom, P. Broekmann, A. Irabien, G. Díaz-Sainz, ACS Catal. 15 (2025) 8753–8767.
[32] M. Ma, S. Kim, I. Chorkendorff, B. Seger, Chem. Sci. 11 (2020) 8854–8861.
[33] C.A. Giron Rodriguez, B.Ó. Joensen, A.B. Moss, G.O. Larrazábal, D.K. Whelligan, B. Seger, J.R. Varcoe, T.R. Willson, ACS Sustain. Chem. Eng. 11 (2023) 1508–1517.
[34] L. Gatti, S. Verhovez, A. Mezza, M. Etzi, S. Stassi, C.F. Pirri, A. Sacco, Adv. Energy Sustain. Res. 6 (2025) e202500312.
[35] U.O. Nwabara, A.D. Hernandez, D.A. Henckel, X. Chen, E.R. Cofell, M.P. de-Heer, S. Verma, A.A. Gewirth, P.J.A. Kenis, ACS Appl. Energy Mater. 4 (2021) 5175–5186.
[36] P. Gonugunta, K. Roohi, M. Soleimani, P.R. Anusuyadevi, P. Taheri, M. Ramdin, Ind. Eng. Chem. Res. 64 (2025) 2113–2122.
[37] M. Chang, W. Ren, W. Ni, S. Lee, X. Hu, ChemSusChem 16 (2023) e202201687.
[38] M. Liu, H. Hu, Y. Kong, I.Z. Montiel, V. Kolivoška, A.V. Rudnev, Y. Hou, R. Erni, S. Vesztergom, P. Broekmann, Appl. Catal. B 335 (2023) 122885.
[39] W. Jung, S.-H. Shin, S. Park, Y. Chae, U. Lee, H.J. Cho, S. Kim, Y.J. Hwang, J. Y. Lee, H. Da Won, ACS Energy Lett. 10 (2025) 620–628.
[40] F. Zeng, H. Deng, M. Zhuansun, W. Teng, Y. Wang, J. Mater. Chem. A 12 (2024) 20990–20998.
[41] S. Emken, K.A. Raman, A. Bauer, V. Karyofylli, E. Jodat, A. Karl, R.-A. Eichel, Adv. Funct. Mater. 36 (2025) e22386.
[42] "HYDRion™ – H2O Electrolysis Membranes", https://ion-power.eu/membranes/ (accessed 25.08.2026).
[43] C. Martens, B. Schmid, H. Tempel, R.-A. Eichel, Green. Chem. 25 (2023) 7794–7806.
[44] C. Martens, B. Schmid, A. Luft, N. Sarioglu, H. Tempel, R.-A. Eichel, Chem. Methods 5 (2025) e202400092.
[45] "ElyFlow PTFE Electrochemical test cell", https://gaskatel.com/shop/voltammetric-cells/electrochemical-test-cell-elyflow-ptfe/ (accessed 25.08.2026).
[46] "Test Cell ElyFlow Electrochemical Test Cell PTFE User Manual", https://gaskatel.com/fileadmin/Redakteur/pdf-Dateien/Bedienungsanleitungen/Manual_TestCell_ElyFlow.pdf (accessed 25.08.2026).
[47] "Counter Electrode for ElyFlow 10 cm2 MMO", https://gaskatel.com/shop/accessories-spare-parts/counter-electrode-for-elyflow-10-cm2-mmo/ (accessed 25.08.2026).
[48] "Sealing for ElyFlow Silicone", https://gaskatel.com/shop/accessories-spare-parts/sealing-for-elyflow-silicone/ (accessed 25.08.2026).
[49] "MH Humidifiers", https://salaera.com/products/mh-humidifiers (accessed 25.08.2026).
[50] "Fundamental Physical Constants — Extensive Listing", https://pml.nist.gov/cuu/pdf/all_2014.pdf (accessed 26.01.2026).
[51] K. Froehlich, T. Hilche, O. Camara, C. König, I. Park, S. Speer, J. Liu, S. Jovanovic, F. Hausen, E. Jodat et al., "Correlating Electrode Morphology with Electrochemical Properties in PEM Water Electrolysis MEAs after variable load cycling", Preprint at 10.26434/chemrxiv.15005691/v1.
[52] M. Bühler, F. Hegge, P. Holzapfel, M. Bierling, M. Suermann, S. Vierrath, S. Thiele, J. Mater. Chem. A 7 (2019) 26984–26995.
[53] B. Mayerhöfer, K. Ehelebe, F.D. Speck, M. Bierling, J. Bender, J.A. Kerres, K.J. J. Mayrhofer, S. Cherevko, R. Peach, S. Thiele, J. Mater. Chem. A 9 (2021) 14285–14295.
[54] B. Mayerhöfer, D. McLaughlin, T. Böhm, M. Hegelheimer, D. Seeberger, S. Thiele, ACS Appl. Energy Mater. 3 (2020) 9635–9644.
[55] S. Favero, I.E.L. Stephens, M.-M. Titirci, Adv. Mater. 36 (2024) e2308238.
[56] I. Arunkumar, R. Gokulapriyan, V. Sakthivel, A.R. Kim, M.S. Oh, J.Y. Lee, S. Kim, S. Lee, D.J. Yoo, ACS Appl. Energy Mater. 6 (2023) 7702–7713.
[57] J. Zhu, A. Pedersen, S. Kellner, R.D. Hunter, J. Barrio, Commun. Chem. 8 (2025) 27.
[58] J. Wang, Y. Zhao, B.P. Setzler, S. Rojas-Carbonell, C. Ben Yehuda, A. Amel, M. Page, L. Wang, K. Hu, L. Shi, et al., Nat. Energy 4 (2019) 392–398.
[59] Y. Lee, S. Kim, Y. Shin, Y. Shin, S. Shin, S. Lee, M. So, T.-H. Kim, S. Park, J.Y. Lee, et al., Adv. Sci. 12 (2025) e2409563.
[60] S. Slade, S.A. Campbell, T.R. Ralph, F.C. Walsh, J. Electrochem. Soc. 149 (2002) A1556.
[61] T. Li, J. Shen, G. Chen, S. Guo, G. Xie, ACS Omega 5 (2020) 17628–17636.
[62] "Product Bulletin P-14 Nafion D520CS/521CS, D2020CS/2021CS", https://www.nafion.com/en/-/media/files/nafion/nafion-d520-d521-d1020-d1021-d2020-d2021-p-14-product-info.pdf (accessed 04.03.2026).
[63] "Technical Data Sheet Aquivion D72-25BS", https://www.fuelcellstore.com/spec-sheets/solvay-aquivion-d72-25bs-dispersion.pdf (accessed 04.03.2026).
[64] "AEMION+® 3rd Generation ELECTROLYSIS OFFERINGS", https://ionomr.com/wp-content/uploads/2023/05/FM-6063-B-Properties-of-3rd-Gen-Aemion-Water-Electrolysis-Membranes-3rd-Gen-2023-01-11.pdf (accessed 19.01.2026).
[65] A. Saccà, V. Baglio, B. Paci, A. Generosi, F.R. Riva, I. Gatto, Mater. Renew. Sustain. Energy 15 (2025) 4.
[66] P. Guan, J. Lei, X. Liu, K. Xu, S. Pei, H. Ding, Y. Zou, W. Feng, F. Liu, Y. Zhang, Chem. Mater. 34 (2022) 7845–7857.
[67] K.-S. Moon, H. Dong, R. Maric, S. Pothukuchi, A. Hunt, Y. Li, C.P. Wong, J. Electron. Mater. 34 (2005) 168–175.
[68] S.K. Volkman, S. Yin, T. Bakhishev, K. Puntambekar, V. Subramanian, M.F. Toney, Chem. Mater. 23 (2011) 4634–4640.

[69] R. Zhang, K.-S. Moon, W. Lin, C.P. Wong, J. Mater. Chem. 2010 (2018) *20*.
[70] Y. Hu, Y. Wang, Y. Yao, Mater. Today Commun. 34 (2023) 105292.
[71] Y.P. Khanna, J. Mater. Sci. Lett. 7 (1988) 817–818.
[72] I. Moussallem, S. Pinnow, N. Wagner, T. Turek, Chem. Eng. Process. Process. Intensif. 52 (2012) 125–131.
[73] J. Osiewacz, M. Löffelholz, B. Ellendorff, T. Turek, J. Power Sources 603 (2024) 234430.
[74] Y.M. Maombi, N.H. Huy Tran, P. Jain, W. Fan, Z. Chen, ACS Sustain. Chem. Eng. 13 (2025) 21030–21039.
[75] A. Ameri, J. Chem. Eng. Data 70 (2025) 766–786.
[76] S. de Angelis, T. Schuler, M. Sabharwal, M. Holler, M. Guizar-Sicairos, E. Müller, F. N. Büchi, Sci. Rep. 13 (2023) 4280.
[77] D. Hoffmeister, S. Finger, L. Fiedler, T.-C. Ma, A. Körner, M. Zlatar, B. Fritsch, K. W. Bodnar, S. Carl, A. Götz, et al., Adv. Sci. 11 (2024) e2402991.
[78] H. Ren, Y. Teng, X. Meng, D. Fang, H. Huang, J. Geng, Z. Shao, J. Power Sources 506 (2021) 230186.
[79] R.D. Giles, J.A. Harrison, H.R. Thirsk, J. Electroanal. Chem. Interfacial Electrochem. 22 (1969) 375–388.
[80] D.A. Brevnov, T.S. Olson, Electrochim. Acta 51 (2006) 1172–1177.
[81] H. Hua, Y. Liu, D. Wang, Y. Li, Anal. Chem. 90 (2018) 9677–9681.
[82] D.M. Morales, M. Risch, J. Phys. Energy 3 (2021) 34013.
[83] M. Schalenbach, V. Selmert, A. Kretzschmar, L. Raijmakers, Y.E. Durmus, H. Tempel, R.-A. Eichel, Phys. Chem. Chem. Phys. 26 (2024) 14288–14304.
[84] H. Hoffmann, M. Kutter, J. Osiewacz, M.-C. Paulisch-Rinke, S. Lechner, B. Ellendorff, A. Hilgert, I. Manke, T. Turek, C. Roth, Ees. Catal. 2 (2024) 286–299.
[85] A. Ozden, F. Li, F.P. García de Arquer, A. Rosas-Hernández, A. Thevenon, Y. Wang, S.-F. Hung, X. Wang, B. Chen, J. Li, et al., ACS Energy Lett. 5 (2020) 2811–2818.
[86] S. Agnihotri, S. Mukherji, S. Mukherji, Nanoscale 5 (2013) 7328–7340.
[87] E.R. Cofell, U.O. Nwabara, S.S. Bhargava, D.E. Henckel, P.J.A. Kenis, ACS Appl. Mater. Interfaces 13 (2021) 15132–15142.
[88] M. Duarte, B. de Mot, J. Hereijgers, T. Breugelmans, ChemElectroChem 6 (2019) 5596–5602.
[89] W. Yin, L. Yuan, H. Huang, Y. Cai, J. Pan, N. Sun, Q. Zhang, Q. Shu, C. Gu, Z. Zhuang, et al., Chin. Chem. Lett. 35 (2024) 108351.
[90] J.T. Hinatsu, M. Mizuhata, H. Takenaka, J. Electrochem. Soc. 141 (1994) 1493–1498.
[91] X. Ren, T.D. Myles, K.N. Grew, W.K.S. Chiu, F, J. Electrochem. Soc. 162 (2015) 1221–F1230.
[92] L. Olivieri, H. Aboukeila, M. Giacinti Baschetti, D. Pizzi, L. Merlo, G.C. Sarti, J. Membr. Sci. 542 (2017) 367–377.
[93] K. Papchenko, S. Kentish, M.G. de Angelis, Polymers 17 (2025) 1581.
[94] C. Kim, J.C. Bui, X. Luo, J.K. Cooper, A. Kusoglu, A.Z. Weber, A.T. Bell, Nat. Energy 7 (2022) 116.